

Numerical simulation and experimental study of emulsification in a narrow-gap homogenizer

H. Steiner^{a,*}, R. Teppner^a, G. Brenn^a, N. Vankova^b, S. Tcholakova^b, N. Denkov^b

^a*Institute of Fluid Mechanics and Heat Transfer, Graz University of Technology, Inffeldgasse 25/F, 8010 Graz, Austria*

^b*Laboratory of Chemical Physics and Engineering (LCPE), Faculty of Chemistry, University of Sofia, 1 James Bourchier Blvd., Sofia 1164, Bulgaria*

Received 23 October 2005; received in revised form 1 March 2006; accepted 14 April 2006

Available online 28 April 2006

Abstract

The present experimental and theoretical study investigates the fragmentation of the oil phase in an emulsion on its passage through a high-pressure, axial-flow homogenizer. The considered homogenizer contains narrow annular gap(s), whereupon the initially coarse oil drops break into fine droplets. The experiments were carried out using either a facility with one or two successive gaps, varying the flow rate and the material properties of the dispersed phase. The measured drop size distributions in the final emulsion clearly illustrated that the flow rate, as well as the dispersed-phase viscosity, and the interfacial tension can significantly affect the drop size after emulsification. The larger mean and maximum drop diameters obtained for the homogenizer with one gap in comparison to those obtained with two gaps (at the same Reynolds number and material parameters of the emulsion phases), highlighted the strong relevance of the flow geometry to the emulsification process. The numerical simulation of the carrier phase flow fields evolving in the investigated homogenizer was proven to be a very reliable method for providing appropriate input to theoretical models for the maximum drop size. The predictions of the applied droplet breakup model using input values from the numerical simulations showed very good agreement with the experimental data. In particular, the effect of the flow geometry—one-gap versus two-gaps design—was captured very well. This effect associated with the geometry is missed completely when using instead the frequently adopted concept of estimating input values from very gross correlations. It was shown that applying such a mainly bulk flow dependent estimate correlation makes the drop size predictions insensitive to the observed difference between the one-gap and the two-gaps cases. This obvious deficit, as well as the higher accuracy, strongly favors the present method relying on the numerical simulation of the carrier phase flow.

© 2006 Elsevier Ltd. All rights reserved.

Keywords: Drop breakup; Emulsion; Homogenisation; Modelling; Hydrodynamics; Numerical flow simulation

1. Introduction

The design of new procedures for the fabrication of nano-structured materials is one of the hot topics in the current materials science with a great potential for applications in various modern chemical production technologies (Xia et al., 1999; Velev and Kaler, 2000; Kralchevsky and Nagayama, 2001; Kralchevsky and Denkov, 2001; Caruso, 2004). The fabrication of nano-composites can be based on the production of emulsions, whose finely dispersed droplet phase provides sufficient surface area for adsorption of the nano particles (Velev et al., 1996; Dinsmore et al., 2002).

It is the subject of the present study to investigate the main effects relevant in the emulsification process using a high-pressure, continuous stream homogenizer. The emulsion is stabilized by adding surface active emulsifiers at a sufficiently high concentration to the primary suspension. In such a surfactant-rich regime the rate of recoalescence of the newly formed drops during emulsification is low, and the final drop size distribution is determined primarily by the hydrodynamic conditions in the underlying flow. The fine droplets highly dispersed in the final emulsion could serve then as templates for the fabrication of the nano-composites.

There exist various techniques of emulsification. A common feature of these procedures is that they involve an interplay between capillary and hydrodynamic forces, which determine the final outcome of the emulsification process. In all techniques

* Corresponding author. Tel.: +43 316 873 7344; fax: +43 316 873 7356.
E-mail address: steiner@fluidmech.tu-graz.ac.at (H. Steiner).

the drop breakage is promoted by a strong deformation of the primary droplets in the coarse premixture of the immiscible continuous and dispersed phases fed into the homogenizer.

Depending on the governing flow regime, three types of forces can be identified which may dominate the process of droplet fragmentation: the viscous shear forces, the form drag forces, and the inertial forces. Their relevance can be decided by the magnitude of drop-size based Weber number $We_d = \rho_c U_{\text{ref}}^2 d / \sigma$ and Reynolds number $Re_d = \rho_c U_{\text{ref}} d / \mu_c$. The Weber number relates the inertial and the surface tension forces, while the Reynolds number relates the inertial to the viscous forces, involving the density of the continuous carrier phase ρ_c , the drop size d , and some reference velocity U_{ref} . At low Weber numbers, where the inertial forces are negligibly small, the droplet deformation and breakup is dominated by the viscous shear forces and the form drag forces. The shear forces prevail in the Stokes flow regime with very low Reynolds numbers of the order of unity. The form drag forces become dominant at higher, but still subcritical, Reynolds numbers, where the flow separation significantly affects the pressure acting on the drop surface. The drop breakage caused by these two mechanisms is typically realized in laminar pipe flow configurations and colloid mills (Walstra, 1983; Stone, 1994). At high Weber numbers typically found in strongly turbulent flows the deformation and breakup of the droplets is mainly due to dynamic pressure forces associated with the turbulent fluctuations of the velocity of the carrier phase. This kind of breakup mechanism, which is basically driven by inertial forces, is frequently utilized in emulsifiers with stirring or shaking devices to enhance the turbulent motion.

The present work investigates the case of droplet fragmentation in the turbulent flow regime. The considered Reynolds numbers based on the bulk flow conditions of the carrier phase in the most active emulsification zone are of the order of 10^4 . The values of the drop-size based Weber and Reynolds numbers We_d and Re_d , described above, are of the order of 10^2 or higher. Rather than using a stirring device, the facility considered here enhances locally the turbulence by forcing the emulsion through a cylindrical pipe containing a strong contraction, which reduces the pipe's cross-sectional area to a narrow annular gap. This device, termed a "narrow-gap homogenizer" in the following, is to some extent similar to high-pressure valve homogenizers, where the emulsion is pumped through a homogenizing valve (Phipps, 1975). However, unlike in the narrow-gap homogenizer considered here, the height of the gap of the valve homogenizers is determined by the aperture between the valve and its seat. Thus, the resulting gap height varies with the lift of the valve adjusting to the flow rate through the device, and it is typically much smaller than the gap height in the present narrow-gap homogenizer. The major advantage of the narrow-gap homogenizer used in the current study is its fixed, well-defined geometry, which allows one to perform precise numerical simulations of the fluid flow inside the homogenizer chamber.

Using a narrow-gap homogenizer with a one- and a two-gaps design, emulsification experiments were carried out to study the influence of the number of gaps, as well as the effects of

hydrodynamic parameters, such as flow rate, viscosity of the dispersed phase, and interfacial tension, on the drop size distribution. Aside from the experimental investigation of the drop size distributions produced, the present study also aims at demonstrating how numerical simulations of the emulsifying flow can help to obtain accurate predictions of the maximum stable drop size from theoretical models. Particularly, the dissipation rate of turbulent kinetic energy, which represents an essential input parameter to the models, is often estimated based on very crude assumptions. The present work instead utilizes the results of the numerical simulation of the flow field inside the emulsifying device to provide more adequate model input values for the average dissipation rate. This approach based on numerical flow simulations finally leads to drop size predictions, which are in a very good overall agreement with the corresponding experimental data.

The present work is organized as follows: the available theoretical expressions for the maximum drop size during emulsification in turbulent flow are briefly discussed in Section 2. The experimental setup and the measuring techniques are described in Section 3. In Section 4, the experimental results are shown. The corresponding numerical simulations and their results are presented in Section 5. The model predictions for the maximum stable droplet diameter are compared against the corresponding experimental data in Section 6. The conclusions follow in Section 7.

2. Emulsification theory in turbulent flows

The mathematical description of the droplet breakup mechanism in turbulent emulsifying flow dates back to the fundamental work by Kolmogorov (1949) and Hinze (1955). This classical concept, also known as the Kolmogorov–Hinze theory, is based on several assumptions. First, non-coalescing conditions are assumed, which is the case if the concentration of the dispersed phase is very low, or, if the coalescence is impeded by the addition of surfactants. Second, the maximum stable size of the drops d_{max} is assumed to be much larger than the Kolmogorov length scale

$$\eta = \left(\frac{\mu_c^3}{\rho_c^3 \varepsilon} \right)^{1/4}, \quad (1)$$

which marks the boundary between the inertial and the viscous subrange in the turbulent energy spectrum. Thus, with

$$d_{\text{max}} \gg \eta \quad (2)$$

lying well within the inertial subrange of the wavelength spectrum of turbulence, the viscous forces in the continuous carrier phase can be neglected. The drop fragmentation is then most conceivably assumed to be driven by the dynamic pressure forces associated with the velocity fluctuations over a distance close to the droplet diameter. Equating the dynamic pressure forces with the counteracting surface tension forces leads to the following force balance for the maximum stable

drop size d_{\max}

$$\frac{\rho_c \bar{v}^2}{2} = C_1 \frac{4\sigma}{d_{\max}} \quad (3)$$

Therein, C_1 represents a constant to be determined from experiments. The estimation of \bar{v}^2 , which represents the average of the squared velocity differences over a distance equal to d_{\max} , is based on the assumption of homogeneous isotropic turbulence. In this case the turbulence in the inertial subrange is solely determined by the dissipation rate ε , which basically represents the turbulent energy transfer per unit mass and unit time. In this inertial subrange, the mean square velocity difference can be written as

$$\bar{v}^2 = C_2 (\varepsilon d_{\max})^{2/3} \quad (4)$$

with the constant $C_2 = 2$ as suggested by Batchelor (1951). Substituting (4) into (3) finally leads to the correlation for the maximum stable diameter

$$\frac{\rho_c \varepsilon^{2/3} d_{\max}^{5/3}}{\sigma} = C_{KH}, \quad (5)$$

according to the Kolmogorov–Hinze theory with the model constant C_{KH} . Although this correlation is basically limited to isotropic homogeneous turbulence, it is nonetheless applied to nonisotropic fields, such as turbulent pipe flows, as well. In such cases the turbulent motion is assumed to be locally isotropic, at least in the range of wavelengths comparable to the size of the largest drops.

It must be noted that the drop size correlation (5) provided by the Kolmogorov–Hinze model is based on the simple static force balance in Eq. (3) between the interfacial tension force and the average turbulent pressure forces acting on the maximum stable drop. Neglecting all dynamic effects, the Kolmogorov–Hinze theory, therefore, does not involve any specific time scale for the drop breakage besides the eddy lifetime $\tau = (d_{\max}^2/\varepsilon)^{1/3}$. The omission of any characteristic breakage time scale can be reasoned by the random nature of the droplet-eddy interaction in a turbulent flow field. It was already argued by Shreekumar et al. (1996) that the interactions between the turbulent eddies and the droplets typically occur rather in a random than a coherent manner. Therefore, it seems to be unlikely that the drops are deformed and finally broken by a successive cooperative action of eddies. It is more likely that the drops break under the influence of one single pressure fluctuation acting for an eddy lifetime. The fact that the Kolmogorov–Hinze model has been proven to give reasonable estimates of d_{\max} for low-viscous drops in many practical applications strongly supports this reasoning. The computational investigation of the breakage process of a drop subject to a single external pressure fluctuation presented by Shreekumar et al. (1996) further showed that the time of breakage decreases as the drop size is increased beyond d_{\max} . This observation also favors the assumption of an infinitely fast breakage process inherent in the static force consideration (3) underlying the Kolmogorov–Hinze model.

The Kolmogorov–Hinze model does not account explicitly for any influence of the viscosity of the dispersed and of the

continuous phase. Therefore, the correlation (5) is strictly valid only for dispersed phase viscosities smaller or equal to the continuous phase viscosity, i.e., $\mu_d \leq \mu_c$, where the drop fragmentation is dominated by the pressure forces associated with the velocity fluctuations and the viscous forces can be neglected (Kolmogorov, 1949). Davis (1985) extended the Kolmogorov–Hinze approach to cases, in which the viscosity of the dispersed phase could be significantly higher than that of the continuous phase by adding a viscous force term to the balance (3). The extended static force balance reads

$$\frac{\rho_c \bar{v}^2}{2} = C_3 \left(\frac{4\sigma}{d_{\max}} + \frac{\mu_d \sqrt{\bar{v}^2}}{d_{\max}} \right). \quad (6)$$

Using Eq. (4) for \bar{v}^2 with $C_2 = 2$ as suggested by Batchelor (1951), a correlation for d_{\max} , which is analogous to Eq. (5), can be written as

$$\frac{\rho_c \varepsilon^{2/3} d_{\max}^{5/3}}{\sigma} = C_{D1} \left[1 + \frac{1}{2^{3/2}} \frac{\mu_d (\varepsilon d_{\max})^{1/3}}{\sigma} \right]. \quad (7)$$

Relying on the empirical data base used in his study, Davis assumed the model coefficient $C_{D1} = 4C_3$ to be unity. It is noted that, from a theoretical point of view, the constant C_{D1} should basically be equal to C_{KH} introduced in Eq. (5), which ensures that Eq. (7) converges to the Kolmogorov–Hinze correlation (5) in the limit $\mu_d \rightarrow 0$ of vanishing dynamic viscosity of the dispersed phase.

In simple wall bounded flow configurations like straight channel flows, an average value for the dissipation rate ε needed in both Eqs. (5) and (7) can be roughly approximated as a function of the total pressure drop per downstream channel length $\Delta p/\Delta x$ due to the friction losses. As it was shown by Karabelas (1978) and Risso (2000), the average dissipation rate for a turbulent flow through a cylindrical pipe with diameter D at a bulk flow velocity U_b reads

$$\varepsilon_b = \frac{\Delta p}{\Delta x} \frac{U_b}{\rho_c} = \frac{f}{2} \frac{U_b^3}{D}. \quad (8)$$

Using the Blasius law for the wall friction coefficient, $f = 0.316 Re^{-1/4}$ with the bulk flow Reynolds number $Re = \rho_c U_b D/\mu_c$, finally yields the expression

$$\varepsilon_b = 0.158 \frac{U_b^3}{D} \left(\frac{\rho_c D U_b}{\mu_c} \right)^{-1/4}. \quad (9)$$

Rather than applying ε_b computed from the rough estimate correlation (9), the present work obtains the model input value for the dissipation rate from the results of the numerical simulation of the flow through the narrow-gap homogenizer described in detail in Section 5 below. Therefore, besides the gain of a detailed insight into the flow field in the considered device, the simulation was mainly motivated to provide a reliable estimate for ε , which represents an essential input into the droplet breakup modelling. Since the maximum stable droplet diameter is basically proportional to the inverse of ε , the region with highest mean dissipation rate can be considered to be relevant

for the distribution of the drop sizes produced by the homogenizer.

3. Materials and experimental methods

3.1. Materials

Three emulsifiers were used in different series of experiments, which ensured different interfacial tensions of the oil-water interface: the nonionic surfactant polyoxyethylene-20 hexadecyl ether (Brij 58, product of Sigma), the anionic surfactant sodium dodecyl sulfate (SDS, product of Acros), and the protein emulsifier sodium caseinate (Na caseinate; ingredient name Alanate 180; product of NXMP). All emulsifiers were used as delivered from the supplier, and their concentrations in the aqueous solutions (1 wt% for Brij 58 and SDS, and 0.5 wt% for Na caseinate) was sufficiently high to suppress drop coalescence during emulsification. All aqueous solutions were prepared with deionized water, which was purified by a Milli-Q Organex system (Millipore). The aqueous phase contained also NaCl (Merck, analytical grade) in the concentration of 150 mM for the Brij 58 and Na caseinate solutions, and 10 mM for the SDS solutions. The protein solutions contained also 0.01 wt% of the antibacterial agent NaN_3 (Riedel-de Haën).

As dispersed phase we used three oils, which differed in their viscosity μ_d : soybean oil with $\mu_d = 50 \times 10^{-3} \text{ Pa s}$ (SBO, commercial product); *n*-hexadecane with $\mu_d = 3.0 \times 10^{-3} \text{ Pa s}$ (product of Merck); and silicone oil with $\mu_d = 95 \times 10^{-3} \text{ Pa s}$ (Silikonöl AK100, product of BASF). The soybean oil and *n*-hexadecane were purified from surface-active ingredients by passing these oils through a glass column, filled with Florisil adsorbent (Gaonkar and Borwankar, 1991). The silicone oil was used as delivered from the supplier.

3.2. Design of the homogenizer and emulsification procedure

All emulsions were prepared by using a custom-made “narrow-gap” homogenizer with an axially symmetric cylindrical mixing head (Tcholakova et al., 2003, 2004). The mixing head contained a processing element, which had either one or two consecutive narrow gaps, through which the oil-water mixture was passed under pressure, see Fig. 1(a). Both processing elements used (see Figs. 1b and c), contained gaps with a gap height of 395 μm and length of 1 mm. More details of the exact geometry of the homogenizing device are presented in Section 5 below.

The final oil-in-water emulsions were produced applying a two-step procedure. First, a coarse emulsion was prepared by hand-shaking a vessel, containing 20 ml oil and 1980 ml surfactant solution, such that a total volume of 2000 ml with a dispersed-phase volume fraction $\Phi = 0.01$ was obtained. In the second homogenization step, the emulsion was pumped through the narrow-gap homogenizer in a series of consecutive passes. The driving pressure for this process was provided by a gas bottle containing pressurized nitrogen N_2 . A pressure transducer was mounted close to the homogenizer inlet to measure accurately the driving pressure, which allowed us to control it dur-

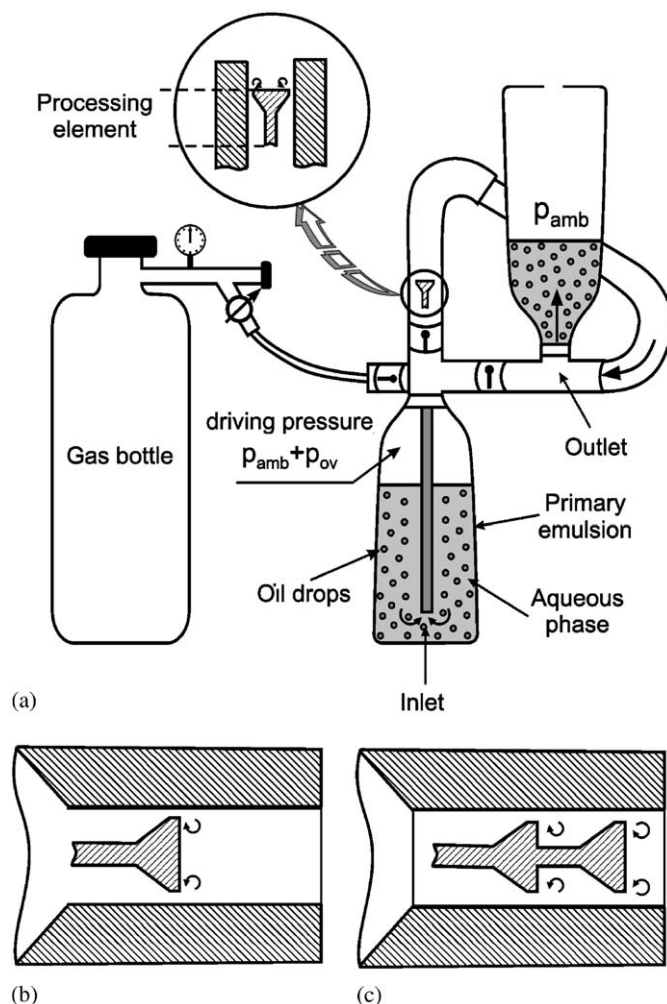


Fig. 1. (a) Schematic sketch of the used homogenizer, which was equipped with a processing element; (b) with one gap; (c) with two gaps. An initial oil-water premix was prepared by hand-shaking and introduced in the homogenizer before starting the actual emulsification experiment, as described in Section 3.2. The drop sizes reported in the paper are measured after 100 passes of the emulsion through the homogenizer head to achieve a steady-state drop-size distribution.

ing the experiment with an accuracy of $\pm 500 \text{ Pa}$. The driving pressure was adjusted in advance (in precursive experiments) to ensure the desired flow rate during the actual emulsification experiments.

After passing through the homogenizer, the oil-water mixture was collected in a container attached to the outlet of the equipment. Then the gas pressure at the inlet was released, and the emulsion was poured back into the container attached to the inlet by using a by-pass tube. Then the gas pressure at the inlet was increased again to the desired value, and the emulsion was allowed to make another pass through the homogenizer.

Previous experiments had shown that a steady-state drop size distribution is achieved after approx. 50 passes of the emulsion through the homogenizer (Tcholakova et al., 2003). Therefore, we always performed 100 consecutive passes of the emulsion through the homogenizer in these experiments to ensure a steady-state size distribution. The experiments were carried

out at the flow rates $Q = 0.145 \pm 0.001$ and 0.092 ± 0.001 ($10^{-3} \text{ m}^3 \text{ s}^{-1}$).

3.3. Determination of the drop size distribution

The drop size distribution in the obtained final emulsions was determined by video-enhanced optical microscopy (Tcholaková et al., 2003, 2004; Denkova et al., 2004). The oil drops were observed and video-recorded in transmitted light by means of the microscope Axioplan (Zeiss, Germany), equipped with the objective Epiplan, $\times 50$, and connected to a CCD camera (Sony) and VCR (Samsung SV-4000). The diameters of the oil drops were measured one by one, from the recorded video-frames, by using a custom-made image analysis software, operating with Targa + graphic board (Truevision, USA). For all samples, 3000 drops were measured. A detailed description of the sampling procedure and the precautions undertaken to avoid artifacts in the used optical measurements is presented in Denkova et al. (2004); the accuracy of the optical measurements is estimated there to be $\pm 0.3 \mu\text{m}$.

Two characteristic drop sizes were determined from the measured drop diameters. The Sauter mean diameter d_{32} , was calculated using the relation

$$d_{32} = \frac{\sum_i N_i d_i^3}{\sum_i N_i d_i^2}, \quad (10)$$

where N_i is the number of drops with the diameter d_i . The second characteristic diameter, d_{v95} , is defined as the value of d for which 95% by volume of the dispersed phase is contained in drops with $d < d_{v95}$. The diameter d_{v95} represents a volume based measure for the maximum drop size, against which the predictions for d_{max} obtained from the breakage models will be evaluated in Section 6 below. The analysis of the experimentally measured drop size data also includes the root mean square values computed as

$$d_{\text{rms}} = \left[\frac{1}{(\sum_i N_i) - 1} \sum_i (N_i d_i - \bar{d})^2 \right]^{1/2} \quad \text{with} \\ \bar{d} = d_{10} = \frac{\sum_i N_i d_i}{\sum_i N_i}, \quad (11)$$

which is used as a measure for the polydispersity of the drop size spectra.

3.4. Measurements of the oil viscosity

The viscosity of soybean oil and *n*-hexadecane was measured using a capillary-type viscometer calibrated with pure water. The viscosity of the silicone oil was measured using a Brookfield Rheoset laboratory viscometer, model LV (Brookfield Engineering Laboratories, Inc.), controlled by a computer. The spindle CP-40 (cone-plate geometry, cone angle = 0.8° and radius 2.4 cm, measured viscosity range 10^{-2} –1 Pa s) was used. The viscosity measurements were performed at a fixed temperature of $25 \pm 0.1^\circ\text{C}$.

3.5. Measurements of the interfacial tension

The oil–water interfacial tension was measured using a drop-shape-analysis of pendant oil drops immersed in the surfactant solutions (Chen et al., 1998). The measurements were performed on a commercial Drop Shape Analysis System DSA 10 (Krüss GmbH, Hamburg, Germany).

3.6. Studied effects

The effects of the following factors on the drop size distribution were experimentally studied:

- (1) design of the processing element (one versus two gaps)
- (2) volumetric flow rate ($Q = 0.092 \times 10^{-3}$ vs. $0.145 \times 10^{-3} \text{ m}^3 \text{ s}^{-1}$)
- (3) viscosity of the dispersed phase ($\mu_d = 3.0 \times 10^{-3}$, 50×10^{-3} , and $95 \times 10^{-3} \text{ Pa s}$)
- (4) interfacial tension (from $\sigma = 5.5 \times 10^{-3}$ to $14 \times 10^{-3} \text{ N m}^{-1}$).

4. Experimental results

All experiments were performed at a high surfactant concentration and a low oil volume fraction of $\Phi = 0.01$ to suppress dynamic drop-drop interactions and drop coalescence during emulsification. Two processing elements, with one gap and with two gaps, were used in parallel series of experiments. Most of the experiments were carried out at the flow rate $Q = 0.145 \times 10^{-3} \text{ m}^3 \text{ s}^{-1}$, and several series of experiments were performed at the lower flow rate $Q = 0.092 \times 10^{-3} \text{ m}^3 \text{ s}^{-1}$ to study the effect of the Reynolds number on the drop size distribution. The measured cumulative volume based drop size distributions are shown in Fig. 2. The cumulative volume fractions Ψ_d , obtained from

$$\Psi_d = \frac{\sum_{d_i \leq d} N_i d_i^3}{\sum_i N_i d_i^3} \times 100 (\%), \quad (12)$$

are plotted against the drop diameter d . The Sauter mean drop diameter d_{32} , the maximum diameter d_{v95} , as well as the size rms values d_{rms} of the measured drop ensembles for all twelve experimental cases considered are summarized in Table 1. It is noted that, since both characteristic diameters d_{32} and d_{v95} exhibit practically the same tendencies in all test cases, they need not be addressed separately. In effect, the discussions of the drop size presented below apply to both characteristic diameters.

4.1. Effect of hydrodynamic conditions (flow rate and number of gaps in the processing element)

As expected, an increase of the flow rate results in smaller droplets if the other conditions are unchanged. This can be clearly seen from Figs. 2c and d, where the cumulative drop size distributions extend to the larger diameters for the lower flow rate (cases 7 and 8, denoted by the dashed lines). In

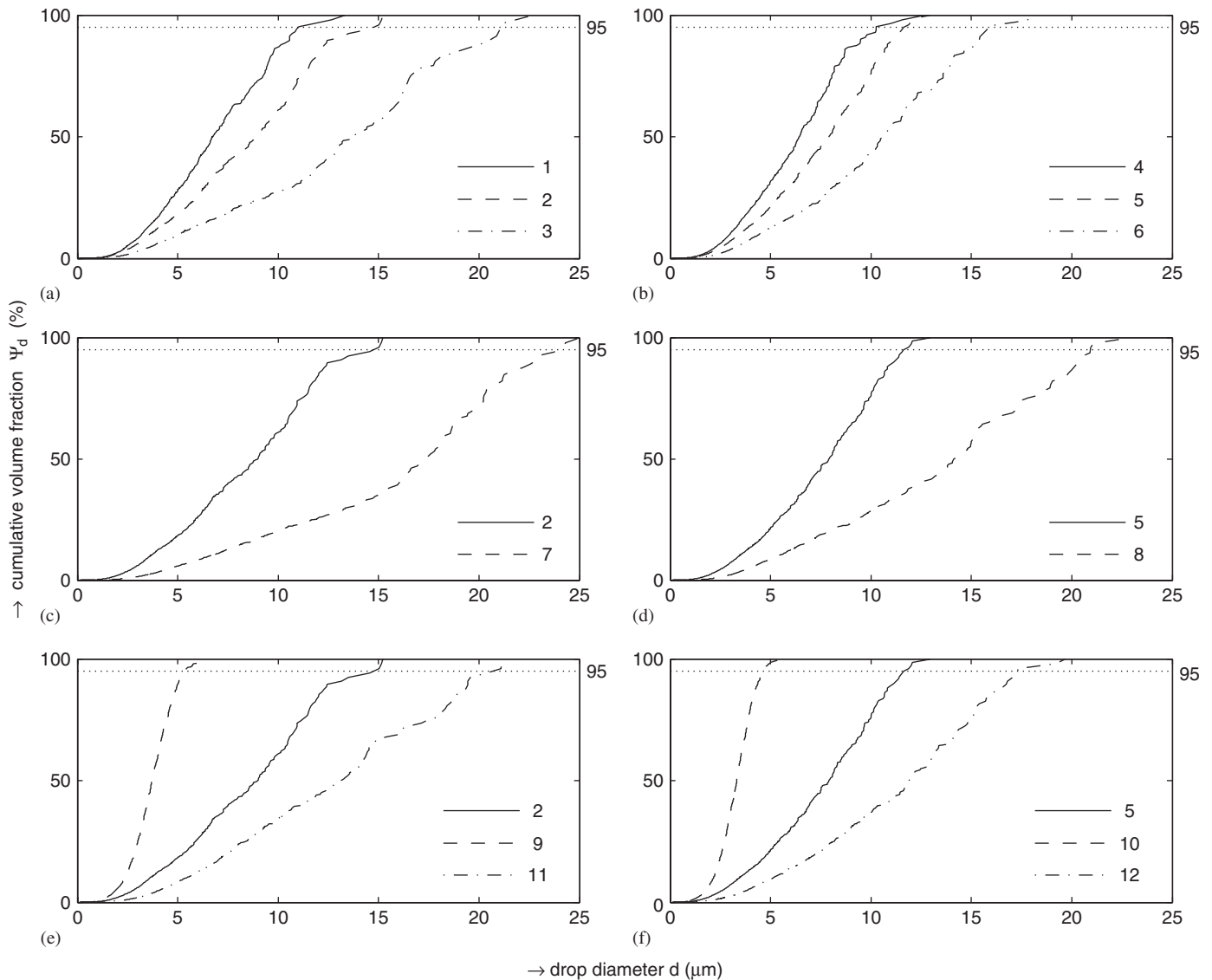


Fig. 2. Measured volume based cumulative drop size distributions Ψ_d (%) versus drop diameter d (μm). The volume based maximum drop diameters $d_{v,95}$ are denoted by the intersections with the horizontal dotted line at $\Psi_d = 95\%$. The subfigures (a), (c), and (e) show results obtained with 1 gap, whereas (b), (d), and (f) show results obtained with two consecutive gaps in the homogenizer head. The various curves in the subfigures (a), (b) compare different surfactants, viz. different interfacial tensions; in (c), (d) different flow rates; and in (e), (f) oils with different viscosities.

effect, the mean drop size is increased by almost a factor of two (from 6.6 to 12 μm for the homogenizer with one gap, and from 6 to 10 μm for the homogenizer with two gaps) when Q is reduced from 0.145×10^{-3} to $0.092 \times 10^{-3} \text{ m}^3 \text{ s}^{-1}$ in the system SBO + Brij 58 (see Table 1, cases 2 and 5 versus cases 7 and 8, respectively). Moreover, the higher rms values d_{rms} indicate a higher polydispersity of the drop sizes spectra at the lower flow rate. This tendency can be seen from the markedly decreased gradients of the corresponding cumulative distribution functions in Fig. 2c and d as well.

The design of the processing element also affects markedly the mean drop size resulting from the emulsification. In all considered cases the mean and the maximum drop sizes produced with the two-gaps element is about 15% smaller as compared to the one-gap element. As seen from Fig. 2, the cumulative drop size distributions lie always somewhat closer to the ordinate

in the two-gaps cases plotted in the right-hand side subfigures than the corresponding one-gap curves plotted in the left-hand side subfigures. The steeper slopes of the distribution curves in line with the smaller rms values d_{rms} make also evident that the drop size spectra produced by the two-gaps design are always less polydisperse than in the one-gap case. It will be shown in the discussion of the numerical simulations of the flow field (see Section 5) that the observed decrease in the drop size can be attributed to the fact that turbulence is further increased in the second gap relative to the first one.

4.2. Effect of the oil viscosity

To study the effect of the oil viscosity μ_d , we produced emulsions with three different oil phases, *n*-hexadecane, soybean oil, and silicone oil. These emulsions were stabilized with the same

Table 1

Experimental results for the Sauter mean drop diameters d_{32} , the volume-based maximum drop diameters d_{v95} , and the number-based rms values of the drop size d_{rms}

Case	viscosity of dispersed phase μ_d (10^{-3} Pa s)	Flow rate Q (10^{-3} m ³ s ⁻¹)	Geometry	Emulsifier and surface tension		d_{32} (μm)	d_{v95} (μm)	d_{rms} (μm)
				Type	σ (10^{-3} N m ⁻¹)			
1	50	0.145	one-gap	SDS	5.5	5.5	11.2	1.9
2	50	0.145	one-gap	Brij 58	7.4	6.6	13.9	2.0
3	50	0.145	one-gap	Na cas.	14	9.7	21.5	2.6
4	50	0.145	two-gaps	SDS	5.5	5.0	10.1	1.7
5	50	0.145	two-gaps	Brij 58	7.4	6.0	11.6	1.9
6	50	0.145	two-gaps	Na cas.	14	8.0	16.0	2.4
7	50	0.092	one-gap	Brij 58	7.4	12.0	23.9	3.4
8	50	0.092	two-gaps	Brij 58	7.4	10.0	21.2	2.9
9	3	0.145	one-gap	Brij 58	7	3.3	5.4	1.2
10	3	0.145	two-gaps	Brij 58	7	3.0	4.6	1.1
11	95	0.145	one-gap	Brij 58	10.3	9.6	20.7	2.9
12	95	0.145	two-gaps	Brij 58	10.3	8.9	17.4	2.7

The twelve experimental test cases are specified by varying type of the dispersed phase (soybean oil in cases 1 through 8, *n*-hexadecane in cases 9 and 10, silicone oil in cases 11 and 12), flow rate Q , geometry of the processing element, and type of the surface-active emulsifier.

surfactant, 1 wt% Brij 58, to ensure similar (though not exactly the same) interfacial tensions σ . As seen from Figs. 2e and f and Table 1, a higher viscosity of the dispersed phase results in larger drops for a given flow rate. This increase of the mean and the maximum drop sizes is again accompanied by a considerably increased polydispersity, which is clearly manifested in the more gently rising distribution curves and the higher rms values d_{rms} . The viscous dissipation inside the drops during their breakup can evidently play a significant role and should be taken into account in the data interpretation as well as in the modeling of the droplet breakup. For example, in the emulsions produced with the two-gaps element, the smallest Sauter mean drop diameter $d_{32} = 3.0 \mu\text{m}$ is observed for *n*-hexadecane with $\mu_d = 3 \times 10^{-3}$ Pa s, whereas largest diameter $d_{32} = 8.9 \mu\text{m}$ is obtained for silicone oil with $\mu_d = 95 \times 10^{-3}$ Pa s (see Table 1, cases 10 and 12, respectively). It can be further observed that the ratio of the characteristic diameters d_{32}/d_{v95} is about 0.6 in the cases with moderate viscosity, $\mu_d = 3 \times 10^{-3}$ Pa s (cases 9 and 10), while it lies around 0.5 in the other cases with considerably higher viscosities, $\mu_d = 50 \times 10^{-3}$ and 95×10^{-3} Pa s. This observation is well in line with the findings by Calabrese et al. (1986) obtained in stirred-tank experiments. Although the work done by the viscous forces inside the dispersed phase can evidently dissipate a good deal of the mechanical energy, which has to be supplied by the turbulent motion of the carrierphase to promote the droplet breakup, the viscous heating of the droplets is still negligibly small. The assumption of isothermal flow conditions can be justified by estimating the increase of the temperature due to viscous dissipation inside the annular gap as

$$\Delta T_{\text{gap}} = \frac{\bar{\epsilon}_{\text{gap}} V_{\text{gap}}}{Q c_p}. \quad (13)$$

Assuming an overall specific heat capacity of $c_p = 4200 \text{ J kg}^{-1} \times \text{K}^{-1}$, the heat-up would be at maximum about $\Delta T_{\text{gap}} \approx 0.004 \text{ K}$ in all considered cases.

4.3. Effect of the interfacial tension

To study the effect of the interfacial tension between the dispersed oil phase and the continuous water phase, we compared the mean drop sizes of emulsions obtained with soybean oil, when using different surface active emulsifiers. As seen from Table 1 (cases 1–3 for the one-gap, and 4 to 6 for the two-gaps geometry), the largest drops were always obtained with Na caseinate ($\sigma = 14 \times 10^{-3} \text{ N m}^{-1}$), whereas the smallest drops were obtained with SDS ($\sigma = 5.5 \times 10^{-3} \text{ N m}^{-1}$). It becomes evident that a higher interfacial tension leads to a larger drop size and to a considerably increased polydispersity, as indicated by the higher rms values d_{rms} . This tendency is also clearly shown by Figs. 2a and b, where the drop size distribution curves with the higher interfacial tensions increase more slowly and extend to larger drop diameters.

4.4. Relation between the driving pressure and the flow rate

The dependence of the driving overpressure p_{ov} against the ambient pressure p_{amb} on the flow rate Q can be deduced from Fig. 3. The data for the pressure loss coefficient ζ shown are obtained by relating the measured driving overpressure p_{ov} to the dynamic pressure $p_{\text{dyn},in} = \rho_c(Q/A_{in})^2/2$ at the inlet of the device with the cross-sectional area $A_{in} = D_{in}^2\pi/4$, with D_{in} being the diameter of the inlet. The Reynolds number representing the flow rate Q on the abscissa is also based on the inlet conditions $Re_{in} = 4\rho_c Q/(D_{in}\pi\mu_c)$. It becomes evident that, due to the passage of the flow through another gap, the pressure loss is significantly higher in the two-gaps case. At a given Reynolds number Re_{in} , specified by the considered flow rate Q , the pressure loss coefficient, and hence the required driving overpressure p_{ov} , is about twice as high in the two-gaps than in the one-gap case. The data can be well represented by empirical power law fits, which are displayed as the corresponding trendlines in Fig. 3 as well. Both lines exhibit a weak

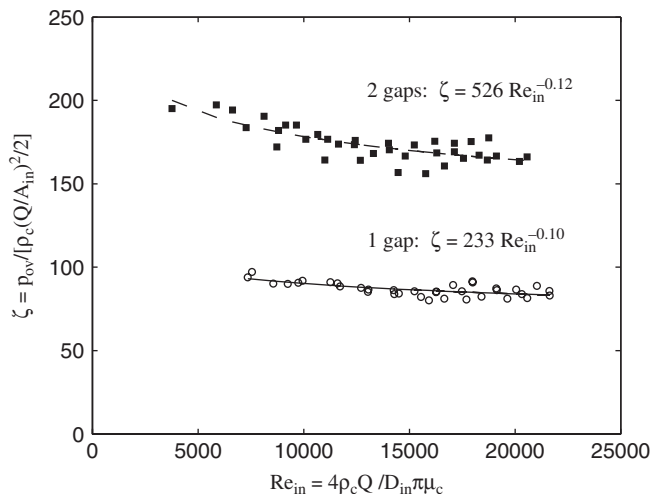


Fig. 3. Pressure loss coefficient ζ of the emulsifier versus Reynolds number based on inlet conditions; the symbols denote the experiments, the solid and the dashed curves represent the trendlines for the one-gap and two-gaps cases, respectively.

dependence on the inverse of the Reynolds number, which is a typical feature of turbulent channel flows.

5. Numerical simulation of the flow through the emulsifier

5.1. Computational domain and boundary conditions

The considered narrow-gap homogenizer consists basically of an axisymmetric channel, which contains a processing element with either one or two consecutive gaps. The computational domain is shown in Fig. 4 including the alternatively used processing elements. The total axial extension of the domain is $L = 500$ mm, the diameter at the inlet is $D_{in} = 13$ mm. In both the one- and the two-gaps cases, the processing element is located at the same axial position in the channel, and the radial height, as well as the outer diameter of the annular gap are always $h = 0.395$ mm and $D_o = 7.34$ mm, respectively. As it is illustrated by the cross-sectional cut A–A in Fig. 4, the processing element's base plate contains six inlet holes, so that there are six planes of symmetry with respect to the circumferential direction θ . Passing through these holes at the base plate, the flow becomes non-axisymmetric, which requires a spatially three-dimensional simulation. The present numerical simulations are carried out on a computational domain bounded by two neighbouring planes of symmetry, which is sufficient to fully capture the three-dimensional flow field associated with the six inlet holes of the base plate. The circumferential extension of the computational flow domain is $\Delta\theta = 30^\circ$, as indicated in the cross-sectional cut A–A in Fig. 4. On the side planes, at $\theta = 0^\circ$ and 30° , symmetry boundary conditions with respect to the circumferential direction θ are applied. At all channel walls and on the surface of the processing element the no-slip boundary condition is applied. At the inlet, a constant inflow velocity is imposed. Its magnitude is set corresponding to the two volumetric flow rates $Q = 0.092 \times 10^{-3}$ and $Q = 0.145 \times 10^{-3} \text{ m}^3 \text{ s}^{-1}$

applied in the experiments. The turbulence intensity at the inlet is set to 10% with respect to the magnitude of the inflow velocity. A von Neumann boundary condition is imposed at the outlet of the device.

Since the volumetric fraction of the dispersed oil phase in the considered oil-in-water emulsion is $\Phi = 0.01$, and is thus very low, all hydrodynamic effects of the dispersed phase on the carrier phase flow are neglected. Accordingly, the working fluid is assumed as one continuous phase with the material properties of water being here $\rho_c = 998.2 \text{ kg/m}^3$ and $\mu_c = 1 \times 10^{-3} \text{ Pa s}$.

The Reynolds number based on the flow conditions inside the gap can be written as $Re = (\rho_c Q D_{hyd}) / (A \mu_c)$, where the hydraulic diameter $D_{hyd} = 4A/W$ involves the cross section A and the wetted perimeter W of the narrow gap. For the two considered volumetric flow rates the Reynolds numbers based on the flow inside the gap are $Re = 8450$ and 13270 , respectively. This indicates that the flow through the gaps can be regarded as turbulent. The three-dimensional numerical calculations were carried out with Fluent 6.1.22. The standard $k-\epsilon$ model with a low-Reynolds number model for the near-wall region was used as turbulence model. The total number of grid points of the numerical grid was 850,000.

5.2. Results of the simulations

In total, four individual cases were simulated, combining the volumetric flow rates $Q = 0.092 \times 10^{-3}$ and $0.145 \times 10^{-3} \text{ m}^3 \text{ s}^{-1}$ with the one-gap and two-gaps geometries of the processing element. The results obtained in these four simulations basically cover all carrier phase flow conditions underlying the whole set of experimental test cases described in Section 4. Since the flow region near the processing element is the most relevant zone for the emulsification process, the present discussion of the numerical results is focused on this region. With the given geometry of the base plate of the processing element, the flow passes through six holes, such that it becomes non-axisymmetric in the wake of the element's inlet section. However, approaching the narrow annular gap located downstream, the flow recovers its circumferential homogeneity, and hence its two-dimensionality. It is evident from Figs. 5a and b that, in the strongly contracted section, the streamwise velocity component become axisymmetric as the downstream position approaches the gap. This feature observed in all simulated cases indicates that the flow is three-dimensional only within a short distance downstream from the base plate, while it is practically axisymmetric in all other regions, including the gap sections. The specification of the position in the θ -direction is therefore omitted in all following descriptions of the results.

Some qualitative insight into the velocity field in the vicinity of the processing element is given in Fig. 6, where exemplarily the velocity vectors obtained for the case with the two-gaps geometry and the higher flow rate are shown. The vector plot illustrates that the flow is strongly accelerated in the radially constricted section upstream from the gaps. Downstream from the backward facing edge of each gap, the flow

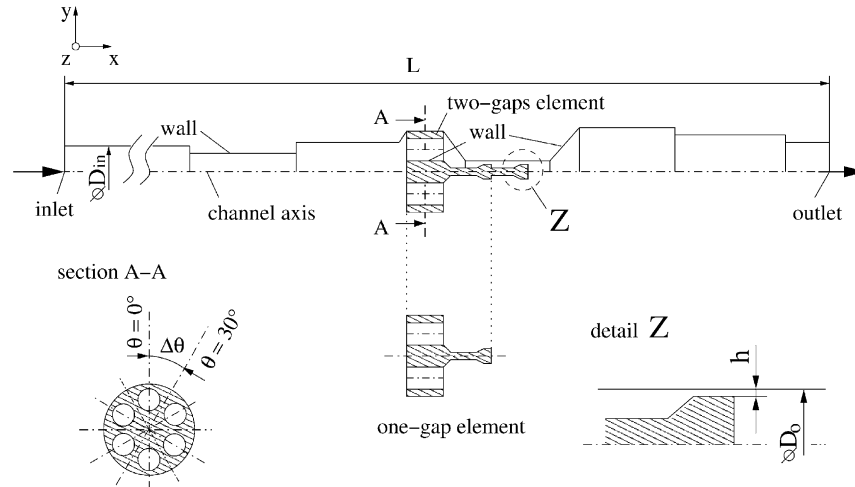


Fig. 4. Meridional section of the computational domain of the homogenizer including the processing elements with one gap and two gaps. The side boundaries of the computational domain are indicated in the cross-sectional view A–A.

separates, and a recirculation zone is formed, as it is indicated by the regions associated with a negative streamwise velocity in the wake of each gap. As will be shown in the following, the strong separation associated with the backward facing step leads to a considerable increase of the turbulence in the wake region. From there the so enhanced turbulence is convected further downstream into the next gap, where it contributes to the gap-to-gap increase of turbulence observed in the numerical results.

The contours of the dissipation rate ε shown in Fig. 7 identify the regions inside the annular gaps and their nearer wakes as the most active zones for the emulsification process, as the ε values are highest there. The comparison of the four considered computational cases reveals for both geometries of the processing element that, in case of the higher flow rate, higher ε levels are achieved and the regions with a high ε extend over wider areas of the flow domain. The peak values of ε always occur in the highly sheared near-wall layers inside the gaps, as shown in Fig. 8, where individual ε profiles at half the streamwise length of the gap located farthest downstream are plotted over the wall normal coordinate. The left end of the curves refers to the inner wall, and the right end to the outer wall of the gap. It is noted that the ε profiles obtained in the first gap of the two-gaps element (not shown in Fig. 8) practically coincide with those shown here for the one-gap element. This coincidence is not surprising due to the identical inflow conditions upstream from the first gap and the expectedly very little effect from the flow downstream. It can be also observed that in the two-gaps case the ε profiles of the second gap lie always considerably above the corresponding profiles of the one-gap case. Forcing the flow through a second gap obviously leads to a further increase of the turbulent dissipation rate. This effect associated with the number of gaps is certainly of relevance in the design of processing elements, whenever highest possible turbulent dissipation rates are attempted to promote droplet breakage. However, as shown in Fig. 3, the pressure loss is almost twice as high in the two-gaps case. This pressure loss penalty, together with the fact

that there conceivably exists an upper limit for the achievable level of turbulence, must certainly be considered as an important design criterion as well. The determination of the optimum number of gaps, however, is beyond the scope of the present study.

6. Comparison of model predictions for the drop size with experimental data

As outlined in Section 3, the turbulent energy dissipation rate ε represents a key input quantity to the models proposed for the maximum stable drop size in turbulent emulsifying flows. The present work attempts to provide a most reliable value for ε from the numerical flow simulations of the narrow-gap homogenizer at hand. Since in all models considered here the maximum stable droplet diameter is basically proportional to the inverse of $\varepsilon^{2/5}$, it is conceivable to assume the region with the highest mean dissipation rate to be the relevant for the resulting drop size distribution produced by the homogenizer. The numerical results revealed that the highest levels of ε occur inside the gap located farthest downstream. Therefore, the volume average of the numerically computed ε field over the annular volume of the gap located farthest downstream

$$\bar{\varepsilon}_{\text{gap}} = \frac{1}{V_{\text{gap}}} \int_{V_{\text{gap}}} \varepsilon \, dV \quad (14)$$

is considered to be the most appropriate input value to the correlations for the determination of the maximum droplet diameter, Eqs. (5) or (7). The volumetric averages obtained for the four considered cases are listed in Table 2. Since in the two-gaps cases the average values in the second gap are always higher than those in the one-gap cases, it becomes evident that applying a second gap leads to an increase of the turbulent dissipation rate.

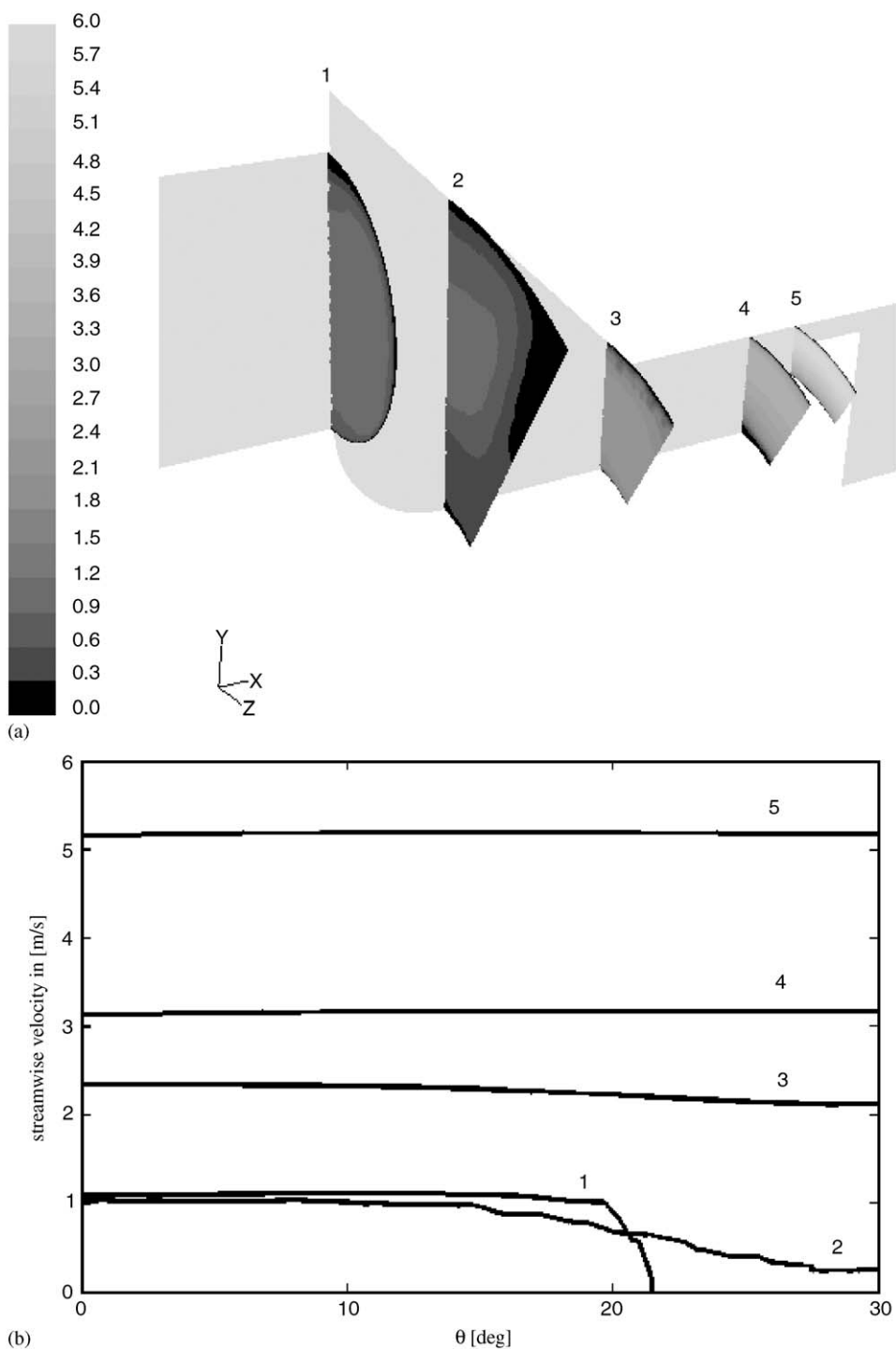


Fig. 5. (a) Contours of the streamwise velocity component ($=x$ direction) in ms^{-1} on cross-sectional planes at successive downstream positions between one inlet hole of the processor element's base plate and the annular gap; one-gap geometry, flow rate $Q = 0.092 \times 10^{-3} \text{ m}^3 \text{ s}^{-1}$. (b) Streamwise velocity at constant radial distance from the axis (midway between the radial lower and upper boundaries) plotted over the circumferential coordinate θ . The numbers refer to the five successive downstream positions shown in (a).

It can be seen from the experimental conditions listed in Table 1 that the viscosity of the dispersed phase μ_d strongly exceeds the value of the aqueous continuous phase μ_c in most of the experimentally investigated cases. Therefore, the correlation given by Eq. (7), which was proposed by Davis (1985)

and is applicable even at high viscosity ratios, $\mu_d/\mu_c \gg 1$, is used here for the prediction of the maximum diameter d_{max} .

Fig. 9 illustrates the good agreement between the scaling, on which the linear correlation (7) is based, and the experimental

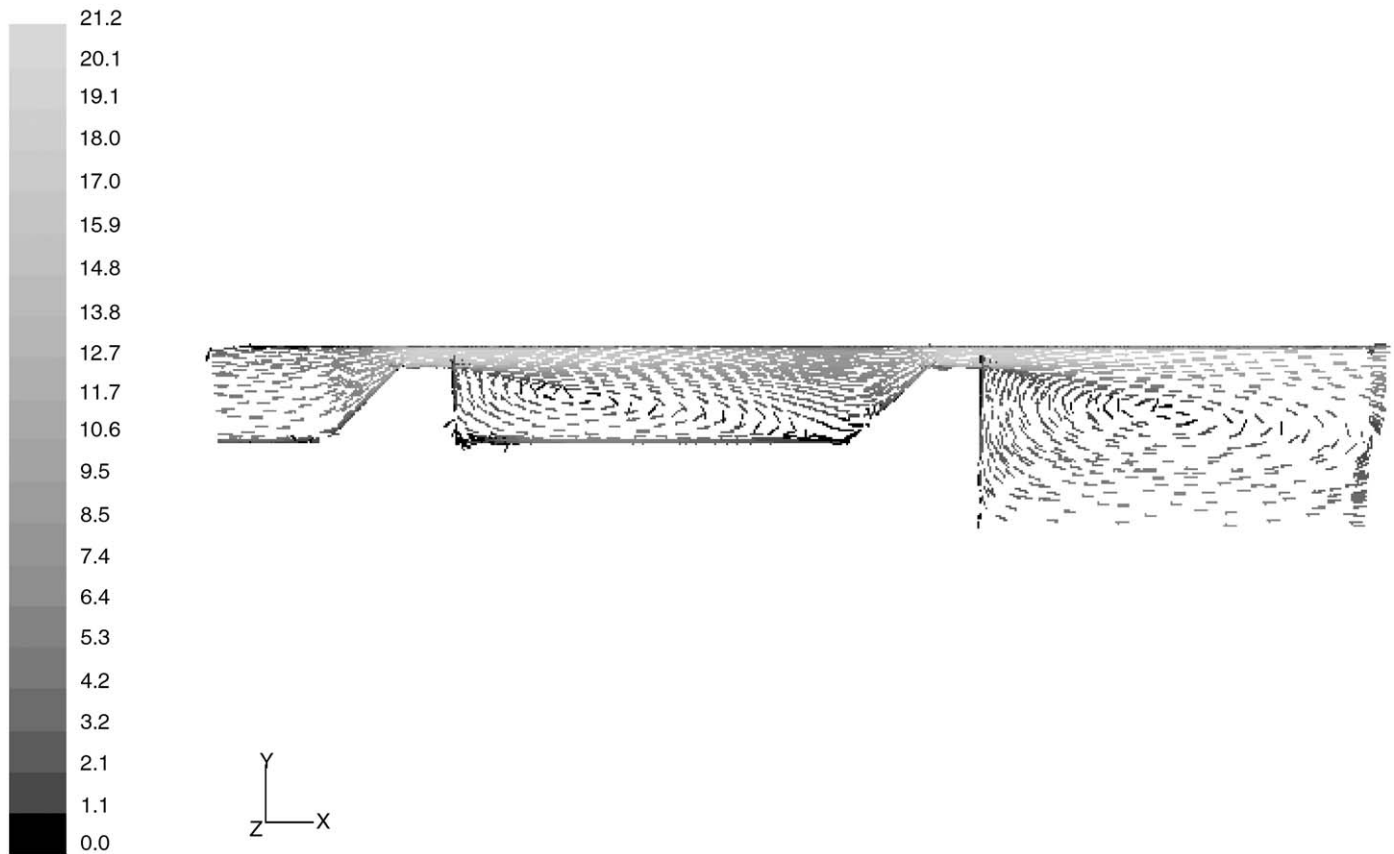


Fig. 6. Velocity vectors for the volumetric flow rate $Q = 0.145 \times 10^{-3} \text{ m}^3 \text{ s}^{-1}$ in the two-gaps geometry. All shown vectors have a constant length, the magnitude of the velocity in m s^{-1} is denoted by the gray-scale.

data. The shown experimental data for all test cases are cast into the two non-dimensional groups of Eq. (7), where the measured values $d_{v,95}$ are used for d_{\max} , and the simulation-based values $\bar{\varepsilon}_{\text{gap}}$ are used for ε . The non-dimensionalized group involving the maximum drop size, which is plotted on the ordinate, evidently exhibits an approximately linear increase with the non-dimensional group representing the dispersed phase viscosity, plotted on the abscissa, as suggested by correlation (7). The shown solid line represents the best fit of this correlation to the data obtained by setting the parameter $C_{D1} = 0.78$. In order to elucidate the effect of the parameter modification with respect to Davis' original value, the line-fit obtained with $C_{D1} = 1$ is shown as a dashed line in Fig. 9 as well. Using the modified, non-unity, parameter improves evidently the agreement, particularly in the cases with high viscosity. In Fig. 10 the predictions of the maximum drop size d_{\max} for all test cases obtained with Davis' and the Kolmogorov–Hinze approaches are summarized and compared against the corresponding diameters $d_{v,95}$ obtained from the experiments. The open circles and squares represent the predictions obtained with the parameter setting $C_{D1} = C_{KH} = 0.78$, and using as inputs for the turbulent dissipation rate the simulation-based values $\bar{\varepsilon}_{\text{gap}}$ computed from Eq. (14) in the volume of the farthest downstream gap. The values of $\bar{\varepsilon}_{\text{gap}}$ actually applied to all test cases are listed in Table 3. As expected, the Kolmogorov–Hinze model is not

applicable in most cases, and the underpredictions become unacceptably large as the viscosity ratio μ_d/μ_c increases, which results in an average relative error of about 54.5%. The predictions computed from Davis' approach (7)—denoted by the open circles—show a very good overall agreement with the experiments. The average relative error is about 12.5%. The second term on the RHS of Eq. (7), which accounts for the viscosity of the dispersed phase, leads evidently to very reliable results over a wide range of viscosity ratios, which in the present test cases spans the range 3 (cases 9 and 10) $\leq \mu_d/\mu_c \leq 95$ (cases 11 and 12).

As already noted in Section 2, there is a computationally much less expensive alternative method to provide appropriate model input values for the turbulent dissipation rate ε . Rather than carrying out a numerical simulation of the flow through the homogenizer, this method estimates an input value for ε from rather gross, but computationally inexpensive approximations like Eq. (9). The predictions for d_{\max} , where the input values for ε were provided by such a method, are shown by the asterisks in Fig. 10. They are again obtained with the model correlation Eq. (7) proposed by Davis (1985), but using Eq. (9) to compute the input values for the turbulent dissipation rate. The numerical values ε_b obtained from Eq. (9), which were actually applied to the individual test cases, are listed in Table 3. Using ε_b instead of $\bar{\varepsilon}_{\text{gap}}$ also implies a change in the

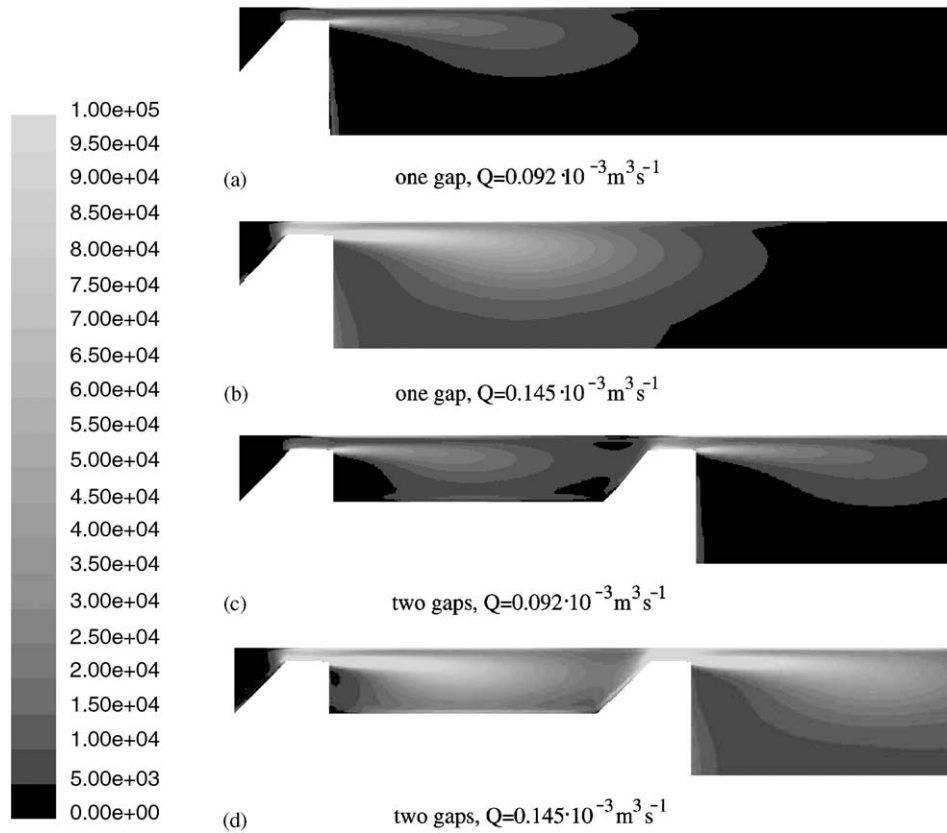


Fig. 7. Contours of the turbulent dissipation rate ε ($\text{m}^2 \text{s}^{-3}$) for both computed geometries and flow rates. For a better discernibility of the individual levels of ε , the ε -scale is clipped, such that regions with $\varepsilon > 10^5 \text{m}^2 \text{s}^{-3}$ appear as white areas.

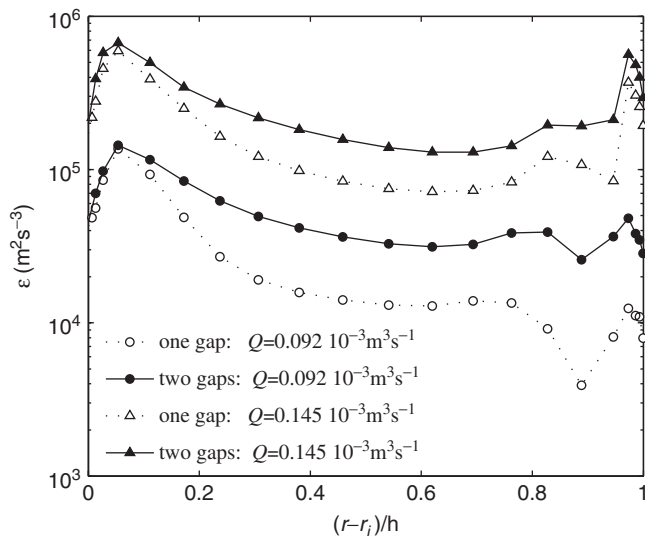
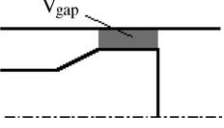
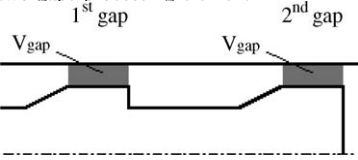


Fig. 8. Profiles of the turbulent dissipation rate ε over the non-dimensional radial coordinate $(r - r_i)/h$ at the streamwise midpoint of the gap located most downstream.

scaling of the non-dimensional groups occurring in the correlation (7), which finally requires to reexamine the setting of the model coefficient C_{D1} . The best fit of the correlation (7) to the

non-dimensionalized data, when scaled with ε_b , is obtained with $C_{D1} = 0.51$. As seen from Fig. 10, applying Davis' approach with ε_b and the modified coefficient C_{D1} still yields a fairly good overall agreement of the predicted diameters with the experiments. The average relative error is about 17.6%. In view of the fact that the overall accuracy of the predictions based on the numerically simulated ε field is not markedly higher (12.5% versus 17.6%), it could be argued that the achieved gain in accuracy does not justify the computational costs for the underlying flow simulation. However, it should not be overlooked that the concept of obtaining model inputs from a numerical simulation of the carrier phase flow brings about the opportunity to capture the spatial variation of all relevant flow quantities associated with the particular geometry of the considered homogenizer. Thus, this concept is not only justified by its basically higher accuracy, but also by its versatility in markedly different flow geometries. The latter feature is in general not provided by correlations like Eq. (9), which simply relate the dissipation rate to the streamwise pressure drop in a fully developed flow through a co-annular channel applying Blasius' law for the friction loss. In the case of the present narrow-gap homogenizer, the dissipation rate given by Eq. (9) varies only with the flow rate Q without any distinction between the one-gap and the multiple-gaps geometries. With the material properties and the flow rate unchanged, this evidently leads to identical predictions for d_{\max} in the one-gap and the corresponding two-gaps

Table 2
Volume average $\bar{\epsilon}_{\text{gap}}$ of the turbulent dissipation rate over the annular gap volumes

one-gap processing element		Flow rate	$\bar{\epsilon}_{\text{gap}}$ ($\text{m}^2 \text{s}^{-3}$)	
		Q ($10^{-3} \text{m}^3 \text{s}^{-1}$)		
		0.092	32706	
		0.145	180247	
two-gaps processing element		Flow rate	1st gap	2nd gap
		Q ($10^{-3} \text{m}^3 \text{s}^{-1}$)	$\bar{\epsilon}_{\text{gap}}$ ($\text{m}^2 \text{s}^{-3}$)	
		0.092	33009	57490
		0.145	189890	274308

The longitudinal section of the gap volume is marked by the shaded areas in the schematic sketches on the left.

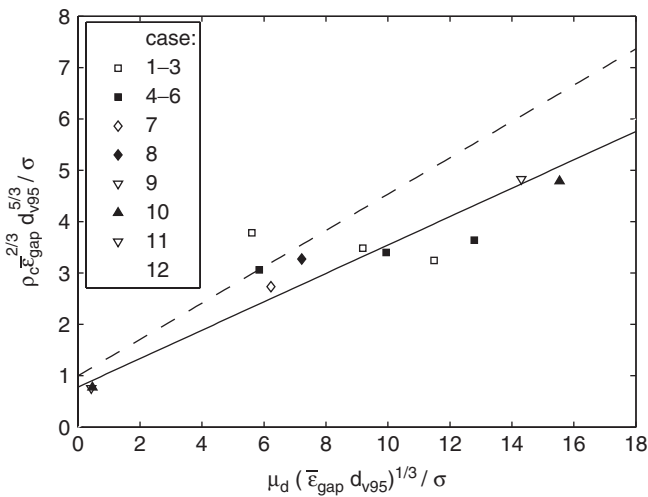


Fig. 9. Scaling of the experimental data cast into non-dimensional groups: $\rho_c \bar{\epsilon}_{\text{gap}} d_{v95}^{5/3} / \sigma$ versus $\mu_d (\bar{\epsilon}_{\text{gap}} d_{v95})^{1/3} / \sigma$; the solid line denotes Davis' correlation (7) with $C_{D1} = 0.78$; the dashed line denotes the same correlation with $C_{D1} = 1$.

cases. It is conceivable that this obvious limitation will become the more stringent, the higher the geometrical complexity of the emulsifier. In configurations which are generally known as highly complex, such as devices with stirrers, or mixers, the pay-off of the numerical simulation of the carrier phase flow is therefore even higher.

7. Conclusions

The present study investigates the emulsifying flow through a narrow-gap homogenizer with varying geometry, flow rate, and material properties. The experiments which were carried

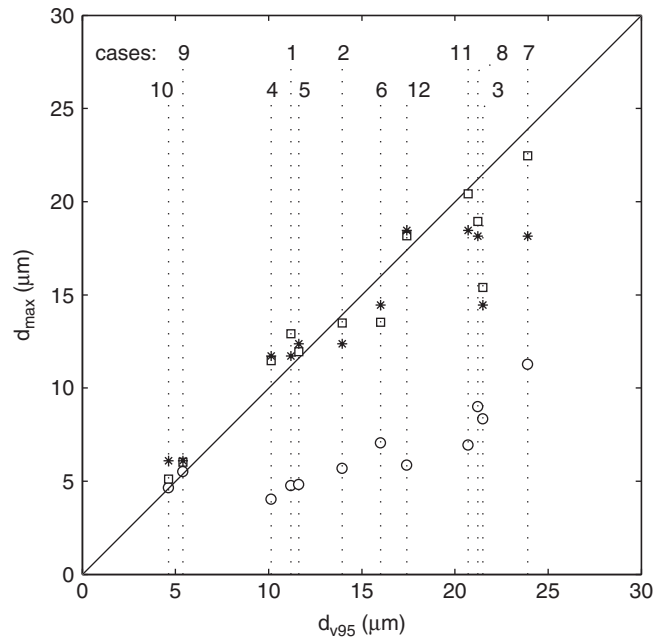


Fig. 10. Predicted maximum droplet sizes d_{max} versus the corresponding experimental values d_{v95} : open circles “o”, Kolmogorov–Hinze model (5); open squares “□”, Davis' correlation (7) using $\bar{\epsilon}_{\text{gap}}$ and coefficient $C_{D1} = 0.78$; asterisks “*”, Davis' correlation (7) using ϵ_b and coefficient $C_{D1} = 0.51$.

out using processing elements with one gap and with two gaps, yielded the following main results.

- For otherwise constant conditions, the homogenizer with two annular gaps produces finer droplets with mean diameters being about 15% smaller as compared to the one-gap design. However, due to the additional friction losses associated with the passage of the suspension through the second gap, the homogenizer with the two-gaps geometry requires a

Table 3

Values of the turbulent dissipation rate $\bar{\varepsilon}_{\text{gap}}$ obtained from Eq. (12) and ε_b obtained from Eq. (9) for use in the 12 test cases as input quantities to the correlations for d_{max}

Case	Flow rate Q ($10^{-3} \text{ m}^3 \text{ s}^{-1}$)	Geometry	$\bar{\varepsilon}_{\text{gap}}$ ($\text{m}^2 \text{ s}^{-3}$)	ε_b ($\text{m}^2 \text{ s}^{-3}$)
1–3, 9, 1	0.145	One-gap	180247	88756
4–6, 10, 12	0.145	Two-gaps	274308	
7	0.092	One-gap	32706	25401
8	0.092	Two-gaps	57490	

significantly higher driving pressure to realize the same flow rate as with the corresponding one-gap geometry.

- As it is expected, the flow rate has a strong effect on the breakage process. A reduction of the flow rate results in final emulsions with considerably larger drop sizes.
- A marked increase of the dispersed-phase viscosity beyond the value of the continuous phase, which was realized by changing the type of the oil phase, affects the resulting drop size significantly. Varying the continuous-phase/dispersed-phase viscosity ratio from $\mu_d/\mu_c = 3$ –95 resulted in an increase of the drop size by a factor of three under otherwise equivalent conditions. Inside a highly viscous dispersed phase, much of the energy supplied from the surrounding continuous flow field is evidently dissipated and is, therefore, not available for the breakup process.
- The surface tension between the continuous and the dispersed phases has a marked effect on the droplet fragmentation, similar to the viscosity ratio. A higher surface tension stabilizes the droplets against breakup, resulting in a larger mean and maximum drop size in the final emulsion.
- It is observed that the droplet spectrum of the final emulsion generally becomes more polydisperse as the forces, which basically counteract the droplet disruption process, such as the surface tension and the dispersed phase viscous forces, increase. On the other hand, an increased level of turbulence, which may be realized by a higher flow rate or by forcing the flow through a second gap, leads to more monodisperse droplet spectra.

The theoretical part of this study includes the numerical simulation of the carrier-phase flow through the narrow-gap homogenizer, the results of which are further used for the modelling of the maximum drop size in the final emulsions. For this part of the study, the main results and conclusions can be summarized as follows:

- Since it is shown by the numerical results that the maximum values of the turbulent dissipation rate ε are achieved inside the gaps, it is reasonable to assume the gap volume to be relevant for the emulsification process.
- Using the averages over the gap volume as input values for ε to the correlation proposed by Davis (1985) for the maximum drop size, predictions in very good agreement with the experimental data are achieved.
- The omission of the effect of the dispersed-phase viscosity yields acceptable accuracy of the predictions for the drop

size only in the low-viscosity cases with $\mu_d/\mu_c = 3$. In all other cases associated with a considerably higher dispersed-phase viscosity, the error is unacceptably large.

- The still frequently adopted alternative concept of applying a gross estimate correlation, which basically depends only on the bulk flow conditions, to compute the turbulent dissipation rate ε as input value to Davis' model produced fairly accurate predictions as well. However, this computationally much less expensive concept is in most cases incapable to capture the effects of the variation of the flow geometry. In the present narrow-gap configuration it yields identical results for the one-gap and the two-gaps geometries. This obvious limitation gives further reason to provide model input data based on the results of numerical simulations of the underlying carrier-phase flow, as it is suggested in the present work. The certainly higher computational costs associated with this method is outweighed by the gain in accuracy, as well as a better versatility to geometrically complex configurations.

Notation

A	cross-sectional area, m^2
c_p	specific heat capacity, $\text{J kg}^{-1} \text{K}^{-1}$
$C_1, C_2, C_3,$ C_4, C_5	constants
d_i	drop diameter in histogram interval i , m
d_{max}	maximum stable drop diameter, m
d_{rms}	root mean square diameter, m
$d_{v,95}$	volumetric maximum drop diameter, m
d_{10}	number based mean drop diameter, m
d_{32}	Sauter-mean drop diameter, m
D	pipe diameter, m
D_{hyd}	hydraulic diameter, m
D_{in}	inlet diameter, m
D_o	outer gap diameter, m
f	friction factor
h	gap height, m
L	total length, m
N_i	number of drops in histogram interval i
p	static pressure, N m^{-2}
Q	volumetric flow rate, $\text{m}^3 \text{ s}^{-1}$
r	radial position, m
r_i	inner annular gap radius, m
Re	Reynolds number
T	temperature, K
U_b	bulk velocity, m s^{-1}
$\overline{v^2}$	mean square velocity difference, m s^{-1}
V_{gap}	gap volume, m^3
W	wetted perimeter, m
x	streamwise (axial) position, m

Greek letters

Δ	difference
ε	turbulent dissipation rate, $\text{m}^2 \text{ s}^{-3}$
ζ	pressure loss coefficient

η	Kolmogorov length scale, m
θ	angle in circumferential direction
μ	dynamic viscosity, Pa s
ρ	density, kg m ⁻³
σ	surface tension, N m ⁻¹
τ	turbulent time scale, s
Φ	volumetric fraction
Ψ_d	cumulative volume fraction

Subscripts

amb	ambient
<i>b</i>	bulk flow
<i>c</i>	continuous phase
<i>d</i>	dispersed phase
ov	over

Acknowledgements

The authors gratefully acknowledge the financial support from the CONEX Program funded by the Austrian Federal Ministry for Education, Science and Culture. The useful discussions with Professor Ivan B. Ivanov and the help in the preparation of the homogenizer by Dr. V. Valchev (both at Sofia University) are also gratefully acknowledged.

References

- Batchelor, G.K., 1951. Pressure fluctuations in isotropic turbulence. *Proceedings of the Cambridge Philosophical Society* 47, 359–374.
- Calabrese, R.V., Chang, T.P.K., Dang, P.T., 1986. Drop breakup in turbulent stirred-tank contactors. Part I: effect of dispersed-phase viscosity. *American Institute of Chemical Engineering Journal* 32 (4), 657–666.
- Caruso, F. (Ed.), 2004. *Colloids and Colloid Assemblies: Synthesis, Modification, Organization and Utilization of Colloid Particles*. Wiley-VCH, Weinheim.
- Chen, P., Kwok, D.Y., Prokop, R.M., del Rio, O.I., Susnar, S.S., Neumann, A.W., 1998. Axisymmetric drop shape analysis (ADSA) and its applications. In: Mobius, D., Miller, R. (Eds.), *Drops and Bubbles in Interfacial Research*. Elsevier, p. 61.
- Davis, J.T., 1985. Drop sizes of emulsions related to turbulent energy dissipation rates. *Chemical Engineering Science* 40 (5), 839–842.
- Denkova, P.S., Tcholakova, S., Denkov, N.D., Danov, K.D., Campbell, B., Shawl, C., Kim, D., 2004. Evaluation of the precision of drop size determination in oil/water emulsions by low resolution NMR spectroscopy. *Langmuir* 20, 11402–11413.
- Dinsmore, A.D., Hsu, M.F., Nikolaidis, M.G., Marquez, M., Bausch, A.R., Weitz, D.A., 2002. Colloidosomes: selectively permeable capsules composed of colloidal particles. *Science* 298, 1006–1009.
- Gaonkar, A.G., Borwankar, R.P., 1991. Competitive adsorption of monoglycerides and lecithin at the vegetable oil–water interface. *Colloids and Surfaces* 59, 331–343.
- Hinze, J.O., 1955. Fundamentals of the hydrodynamic mechanism of splitting in dispersion processes. *American Institute of Chemical Engineering Journal* 1 (3), 289–295.
- Karabelas, A.J., 1978. Droplet size spectra generated in turbulent pipe flow of dilute liquid/liquid dispersions. *American Institute of Chemical Engineering Journal* 24 (2), 170–180.
- Kralchevsky, P.A., Denkov, N.D., 2001. Capillary forces and structuring in layers of colloid particles. *Current Opinion in Colloid & Interface Science* 6, 383–401.
- Kralchevsky, P.A., Nagayama, K., 2001. *Particles at Fluid Interfaces and Membranes*. Elsevier, Amsterdam.
- Kolmogorov, A.N., 1949. On the breaking of drops in turbulent flow. *Doklady Akad. Nauk. U.S.S.R.* 66, 825–828.
- Phipps, L.W., 1975. The fragmentation of oil drops in emulsions by a high-pressure homogenizer. *Journal of Physics D: Applied Physics* 8, 1448–1462.
- Risso, F., 2000. The mechanisms of deformation and breakup of drops and bubbles. *Multiphase Science and Technology* 12, 1–50.
- Shreekumar, Kumar, R., Gandhi, K.S., 1996. Breakage of a drop of inviscid fluid due to a pressure fluctuation at its surface. *Journal of Fluid Mechanics* 328, 1–17.
- Stone, H., 1994. Dynamics of drop deformation and breakup in viscous fluids. *Annual Review of Fluid Mechanics* 26, 65–102.
- Tcholakova, S., Denkov, N.D., Sidzhakova, D., Ivanov, I.B., Campbell, B., 2003. Interrelation between drop size and protein adsorption at various emulsification conditions. *Langmuir* 19, 5640–5649.
- Tcholakova, S., Denkov, N.D., Danner, T., 2004. Role of surfactant type and concentration for the mean drop size during emulsification in turbulent flow. *Langmuir* 20, 7444–7458.
- Velev, O.D., Kaler, E.W., 2000. Structured porous materials via colloidal crystal templating: from inorganic oxides to metals. *Advanced Materials* 12, 531–534.
- Velev, O.D., Furusawa, K., Nagayama, K., 1996. Assembly of latex particles by using emulsion droplets as templates. 1. Microstructured hollow spheres. 2. Ball-like and composite aggregates. *Langmuir* 12, 2374–2384 2385–2391.
- Walstra, P., 1983. Formation of emulsions. In: Becher, P. (Ed.), *Encyclopedia of Emulsion Technology*, vol. I. Basic Theory, Marcel Dekker Inc., New York, Basel, p. 57.
- Xia, Y., Rogers, A.J., Paul, K.E., Whitesides, G.M., 1999. Unconventional methods for fabricating and patterning nanostructures. *Chemical Reviews* 99, 1823–1848.